Article

Enhancement of Guided Wave Detection and Measurement in Buried Layers of Multilayered Structures Using a New Design of *V(z)* Acoustic Transducers

Michaël Lematre * and **Marc Lethiecq**

GREMAN, CNRS, UMR 7347, Université de Tours/INSA Centre Val de Loire, 41000 Blois, France
* Correspondence: michael.lematre@insa-cvl.fr

Abstract: This paper presents the possibility of enhancement of the generation and detection of poorly energetic acoustic-guided waves in multilayered structures using a new design for a $V(z)$ transducer. By defining a modified $V(z)$ transducer composed of segmented piezoelectric elements, the acoustical energy can be directed towards specific angles in such a way as to generate guided waves that are poorly energetic. By comparing the results using this new design to those obtained with a classical $V(z)$ transducer, it is shown that the generation and detection of such waves is greatly improved, especially for poorly energetic waves that belong to a buried layer in a multilayered structure. This is especially seen on the components of the spectra of $V(z)$. The modeling of the modified $V(z)$ signature for a multi-element focused transducer is widely detailed first. Then, in order to illustrate the advantages of our proposed method, a three-layer structure (aluminum/epoxy/steel) is discussed. The interest of this method for the characterization of elastic properties of "buried" layers through specific guided waves that are detected with great difficulty—or even not at all—with a classical $V(z)$ transducer is demonstrated, especially for the A_0 and S_0 modes corresponding to the steel layer inside the three-layer structure. In this study, we also develop a specific tracking method for particular guided waves possessing large phase velocity variations over the considered frequency range, as is the case for the S_0 mode of the steel sub-layer.

Keywords: $V(z)$ acoustic signature; piezoelectric transducers; multilayer structures; guided waves

1. Introduction

Ultrasonic nondestructive testing and evaluation (NDT&E) techniques are the number one method used in industry and are often either preferred to—or used in combination with—other ones, such as Eddy currents, magnetic particles, thermography, or X-rays. Indeed, they allow for the evaluation of mechanical parameters, such as elastic constants, in a wide variety of materials and structures, including bulk and multilayered ones. For the latter, structures are most often characterized through measurements of guided waves velocities, i.e., generalized Lamb wave dispersion curves. When considering their polarization, these guided waves are most often called "guided modes" whose physical properties are used, for example, to characterize the elastic properties of "buried" layers [1–4], interfacial layers [5–11], or coated plates [12–16]. As different mechanical properties influence different guided modes, ideally each mode should be studied separately. Unfortunately, in practice, many different guided modes are often generated depending on the chosen frequency range. To overcome this difficulty, specific signal processing techniques, such as two-dimensional fast Fourier [17] or wavelet transforms [18], need to be developed.

In order to generate and detect guided waves in plates or multilayer samples, planar ultrasonic transducers are often used for material characterization, but other techniques are based on phased-array transducers or focused transducers [19–21]. Among focused transducers, some are designed for use with the $V(z)$ ultrasonic method since it is more practical to use. Furthermore, it often allows for quantitative characterization of several elastic

constants. A typical application of the $V(z)$ method is the determination of the Rayleigh wave velocity [22,23] on thick planar samples with high attenuation in the considered frequency range. Since the method is based on the use of focused transducers that possess a large angular aperture, it has the advantage of avoiding the delicate mechanical angular scanning that is necessary with traditional goniometric set-ups [24,25]. Concerning layered structures, Lamb waves are also widely used to control the health of interfacial bonds or the elastic parameters of the different layers [26,27]. In this case, the $V(z)$ method also has the advantage of allowing the guided modes velocities to be measured at a specific location in the sample. Thus, the $V(z)$ method can detect defects or locally characterize some elastic parameters, which has proven to be very useful for heterogeneous structures. This explains why the use of this acoustic signature is very popular for the characterization of elastic constants in plates, coated materials, or multilayers [28–33]. For example, previous studies discussed the possibility of elastic constant determination with the simplex method of a TiN layer deposited on a MgO substrate and those of a silicon single crystal, by measuring the Surface Acoustic Waves (SAW) velocity with the $V(z)$ method [34].

Unfortunately, there are cases when some guided modes, such as Lamb modes or SAW, are not detectable or are inaccurately measured, which reduces the potential of the $V(z)$ method. Indeed, when different guided modes have phase velocities that are very close to each other and/or if one mode is much more energetic than the others, an overlap of resonance peaks in the spectrum of $V(z)$ curves appears. This situation is illustrated for example in [32], where the phase velocity of S_1 Lamb mode of a bronze plate, for a frequency-thickness product roughly between 2.35 and 2.65 MHz·mm, is not observed with the use of a classical $V(z)$ transducer.

For multilayered structures, the fact that some modes are undetectable can hinder the capabilities of the method, namely when such a mode is sensitive to the specific elastic parameters of a given "buried" layer that needs to be characterized. Thus, this paper aims at the possibility to generate and detect guided modes in a three-layer structure that are too poorly energetic to be observed when using a standard $V(z)$ transducer. To this end, a new type of $V(z)$ transducer we have designed is considered. Its use in the configuration of a multilayer structure shows its great advantage to allow modes that were previously undetectable to be measured and studied, thus allowing elastic constants to be derived from their acoustic wave velocities. A second novelty of this study is the development of a specific procedure to track such modes when they exhibit large phase velocity variations versus frequency.

In Section 2, the non-classical case of modeling of the $V(z)$ signature for a multi-element focused transducer is specifically detailed at first. The formalism of reflection coefficient and associated guided modes is then recalled in Section 2.2, followed by the justification of the chosen spectral representation corresponding to the $V(z)$ signal processing in Section 2.3. Finally, Section 3 presents the results for a three-layer structure by comparison between the determined guided wave velocity values with both the reflection coefficient and dispersion curves. These results allow us to demonstrate the superiority of the multi-element $V(z)$ transducer over the standard one when it comes to detection of poorly energetic guided modes.

2. Theoretical Considerations and Methods

In this section, the interference principle for a classical $V(z)$ transducer is first presented, in order to illustrate how we define the new transducer design that also has to respect the same interference principle. Then, the modelling of $V(z)$ signature for the new transducer design is fully described, before presenting the adopted spectral representation of the $V(z)$ signal processing that allow for results to be compared with reflection coefficient and dispersion curves.

2.1. Principles of V(z) Signature with Single and Multi-Element Focused Transducers

Figure 1a,b show the comparison of the interference principle for a standard $V(z)$ transducer and the new multi-element (or segmented) one, respectively. Figure 1a illustrates the phenomena that occur when defocusing inside the sample is performed. The oscillations that appear in the $V(z)$ curves are mainly due to the interference between the specular echo coming from the center of the piezoelectric element (black ray #1) and the echo coming from the radiation of the guided mode (yellow ray #2), corresponding to a leaky Rayleigh or leaky Lamb wave. As these leaky guided waves radiate their energy into the water at the same angle as the incident angle θ_g corresponding to their generation, they are also detected at this angle. The new $V(z)$ transducer design was imagined in order to allow a specific mode to be favorized. Instead of being made with a single piezoelectric element, it consists of several piezoelectric curved elements with a curvilinear abscissa along the curvature l_i and length Δl, as defined in Figure 1b. The segmented elements are arranged symmetrically on each side of a central one located at the top of the curved surface. In this manner, the interference phenomenon that is the origin of $V(z)$ curves is maintained through the simultaneous excitation of one, or a few, among the elements located around the top of the transducer, with one, or a few, among the elements corresponding to the angle required to generate and detect the targeted guided mode. All elements are assumed to be excited with the same voltage. The top element (or elements) generates and detects the specular echo on the surface of the structure under test, while the other selected element (or elements) generates and detects guided waves. Thanks to this geometrical and electrical configuration, the acoustical energy is sent preferentially in a specific angular region, which allows only a restricted number of guided modes to be generated in their specific frequency ranges. These modes will thus be enhanced, while modes whose generation angles are different will receive very little energy or may even not be generated at all. This will allow modes that are undetectable or inaccurately measured with a classical $V(z)$ transducer of similar size and frequency to be studied. In Section 3, the geometrical parameters chosen both for the classical $V(z)$ transducer (its radius of curvature R_c and half aperture angle θ_{ap}) and the segmented $V(z)$ transducer (the same ones and the length Δl) are given. The z axis origin is chosen at the focus of the transducers. Hence, when the transducer focuses inside the sample, the (z) coordinate of its top surface is negative. The numbering of the piezoelectric elements in Figure 1b is as follows: the central piezoelectric element around the (z) axis is numbered (0), the next one to its right is numbered (1) and symmetrically (-1) for the next one to its left, and so on for all subsequent elements. This numbering will be used in the following theoretical section. These piezoelectric elements have a curvilinear abscissa l_i as indicated in Figure 1b.
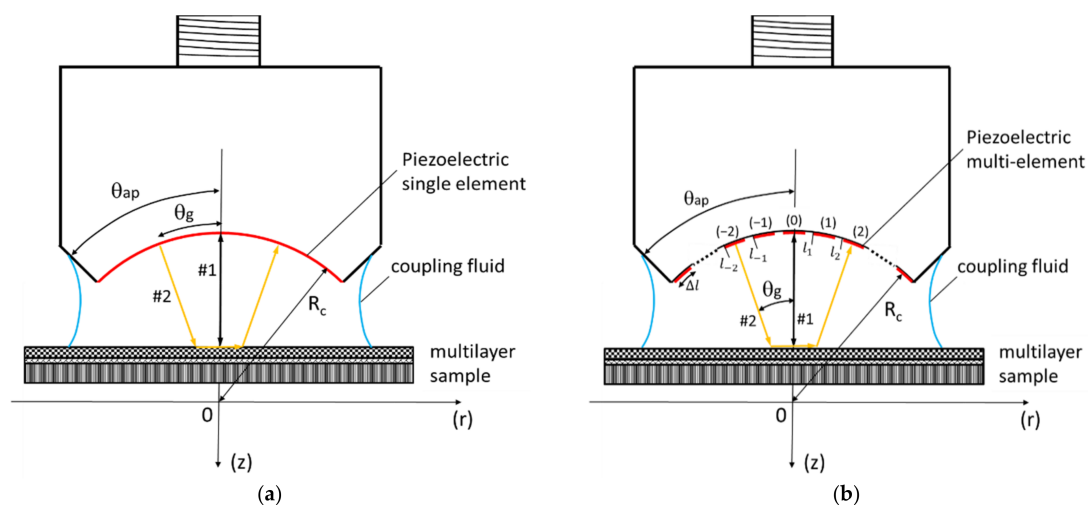

Figure 1. (**a**) Principle of interference with a classical $V(z)$ transducer; (**b**) corresponding scheme with a segmented $V(z)$ transducer.

2.2. V(z) Curve Modelling for Single and Multi-Element Focused Transducers

The most rigorous approach to model the $V(z)$ function consists of using a decomposition of the radiated field of the transducer into an angular spectrum of plane waves. It allows the $V(z)$ function to be expressed as a Fourier integral over the product of characteristic functions that describe both the transducer behavior and the sample response, in the space of wave numbers:

$$V(z) = \int_{-\infty}^{+\infty} U_f^s(k_x) U_s^f(k_x) R(k_x) \exp(-2ik_z z) dk_x,$$ (1)

where:

- k_x is the horizontal component of the wave vector k_0 in the coupling fluid;
- $U_f^s(k_x)$ is the angular spectrum of the incident field of the piezoelectric source (s) defined at the focal plane (f);
- $U_s^f(k_x)$ is the angular spectrum of the transducer response when a plane wave of unit amplitude is emitted from the focal plane (f) to the piezoelectric source (s);
- $R(k_x)$ is the reflection coefficient of the fluid-loaded sample, as a function of the incident wave number component k_x;
- $\exp(-2ik_z z)$ is the phase shift applied to the spectrum $U_s^f(k_x)$ when the surface sample is located at a distance $(-z)$ from the focal plane during defocusing process, where k_z is the vertical component of the wave vector k_0 in the coupling fluid, thus given by $k_z = \sqrt{k_0^2 - k_x^2}$.

In order to characterize both isotropic and anisotropic materials, a line-focused transducer is considered here. Hence, the $V(z)$ transducer possesses a cylindrical shaped piezoelectric element, i.e., without an acoustic lens, for which the focal distance is equal to its radius of curvature. This configuration also implies that the angular spectra $U_f^s(k_x)$ and $U_s^f(k_x)$ are equal.

The angular spectrum of a field is, by definition, the spatial Fourier transform of its complex distribution in a given plane, which here corresponds to a plane perpendicular to the z axis of the transducer. In the case of a field with cylindrical symmetry, the Fourier transform takes the specific form of a cosine transform. The angular spectra $U_f^s(k_x)$ (equal to $U_s^f(k_x)$) is thus evaluated at the focal plane by:

$$U_f^s(k_x) = U_s^f(k_x) = 2 \int_0^\infty u_f^s\left(r_f, z_f\right) \cos\left(k_r r_f\right) dr_f,$$ (2)

where u_f^s is the incident field evaluated at the coordinates $\left(r_f, z_f\right)$ of the focal plane.

When considering the generalized case of a multi-element $V(z)$ transducer, the field at the focal plane u_f^s can be related to the sum of the incident fields emitted on the active surface of the transducer and produced by the piezoelectric elements that are activated. As described in the previous section, and referring to Figure 1b, the interference phenomenon appearing in the $V(z)$ curves is maintained by activating systematically the central element (0), or a few symmetrically located around it—corresponding to the first summation term in Equation (3)—with one, or a few, among the symmetrical elements corresponding to the angle of excitation and detection of the desired guided mode-corresponding to the second and third summation terms in Equation (3). Thus, when considering the activation of N_0 elements around the (z) axis (N_0 is odd) and N consecutive "oblique" elements that start at the element $(-n)$ and symmetrically (n), with $n \neq 0$, the field u_f^s can be expressed by three sums of a function I, such as:

$$u_f^s\left(r_f, z_f\right) = \sqrt{\frac{ik_0}{2\pi}} \left\{ \sum_{i=-(N_0-1)/2}^{+(N_0-1)/2} I + \sum_{i=-n-N}^{-n} I + \sum_{i=n}^{n+N} I \right\},$$ (3)

where the function $I = I\left(r_f, z_f, r_i^s, z_i^s\right)$ defines the field at the coordinates $\left(r_f, z_f\right)$ of the focal plane produced by piezoelectric element (*i*) defined by its left end coordinates (r_i^s, z_i^s):

$$I\left(r_f, z_f, r_i^s, z_i^s\right) = \int_{l_i}^{l_i + \Delta l} u_0^s(r_i^s, z_i^s) \frac{e^{-ik_0 D_f^s}}{\sqrt{D_f^s}} \Omega\left(r_f, z_f, r_i^s, z_i^s\right) dl(r_s). \tag{4}$$

In Equation (4), $dl(r_s)$ is the infinitesimal curvilinear abscissa along the curvature of each piezoelectric element of abscissa l_i, u_0^s is the incident field distribution on the source piezoelectric elements, D_f^s is the distance between the local source point of coordinate (r_s, z_s) and the local evaluation point of coordinate $\left(r_f, z_f\right)$ in the focal plane:

$$D_f^s = \sqrt{\left(r_f - r_s\right)^2 + \left(z_f - z_s\right)^2}, \tag{5}$$

and $\Omega\left(r_f, z_f, r_s, z_s\right)$ is a function called the obliquity factor, defined between each local source point and each local evaluation point in the focal plane, according to Huygens's principle. As the origin of the axes is taken at the center of curvature of the transducer, the obliquity factor is expressed as:

$$\Omega\left(r_f, z_f, r_s, z_s\right) = \frac{1}{2}\left[1 + \frac{r_s\left(r_s - r_f\right) + z_s\left(z_s - z_f\right)}{\sqrt{r_s^2 + z_s^2}\sqrt{\left(r_s - r_f\right)^2 + \left(z_s - z_f\right)^2}}\right]. \tag{6}$$

Equation (1) together with Equations (2)–(6) generalize the expression of the classical $V(z)$ signature obtained with a continuous shaped piezoelectric single element transducer. Thus, one can retrieve this expression by considering in Equation (3) the activation of all the transducer elements and the cancellation of the distance between them. It can also be noted that the modelling of classical $V(z)$ signature has already been validated by comparison between simulations and experimental measurements on a silicon single crystal substrate [34].

Furthermore, the calculation of the acoustic signature $V(z)$ in Equation (1) requires the knowledge of the reflection coefficient R beforehand. In addition, the comparison will be made later between the minima of the modulus of the reflection coefficient R and the associated dispersion curves. Thus, the analytical development details of the calculation of the reflection coefficient, as well as the one of the associated guided waves has been described by authors in a previously published work [35].

The $V(z)$ processing and the choice of its spectral representation are described in the following section. Indeed, its spectral representation can be defined in such a manner that it facilitates the interpretation both with the reflection coefficient and associated dispersion curves.

2.3. V(z) Processing and Associated Spectral Representation

The comparison between the reflection coefficient modulus and guided mode phase velocities (dispersion curves) of the free guided waves is facilitated when choosing to represent them as a function of the incidence angle instead of velocity or wave number. Indeed, according to Snell's law, when identifying the free guided modes to the corresponding leaky ones in the case of the presence of a coupling fluid, each free guided mode can be represented by an equivalent incidence angle θ_0, such as:

$$\theta_0 = \arcsin\left(\frac{V_0}{V_\varphi}\right), \tag{7}$$

where V_0 is the wave velocity in the coupling fluid (here water), and V_φ is the phase velocity of the considered guided wave.

In order to illustrate the $V(z)$ processing and the choice that was made for the associated spectral representation, an example of classical $V(z)$ curve simulated for an aluminum plate of 70 µm thickness and for a frequency of 30 MHz is given in Figure 2a. This material and thickness correspond to the top layer of the layered structure that will be studied below. The oscillations that appear with a spatial periodicity Δz can be related to the phase velocity V_φ of a leaky Lamb mode, using the well-known relationship [34]:

$$V_\varphi = \frac{V_0}{\sqrt{1 - \left(1 - \frac{V_0}{2f\Delta z}\right)^2}}.$$ (8)

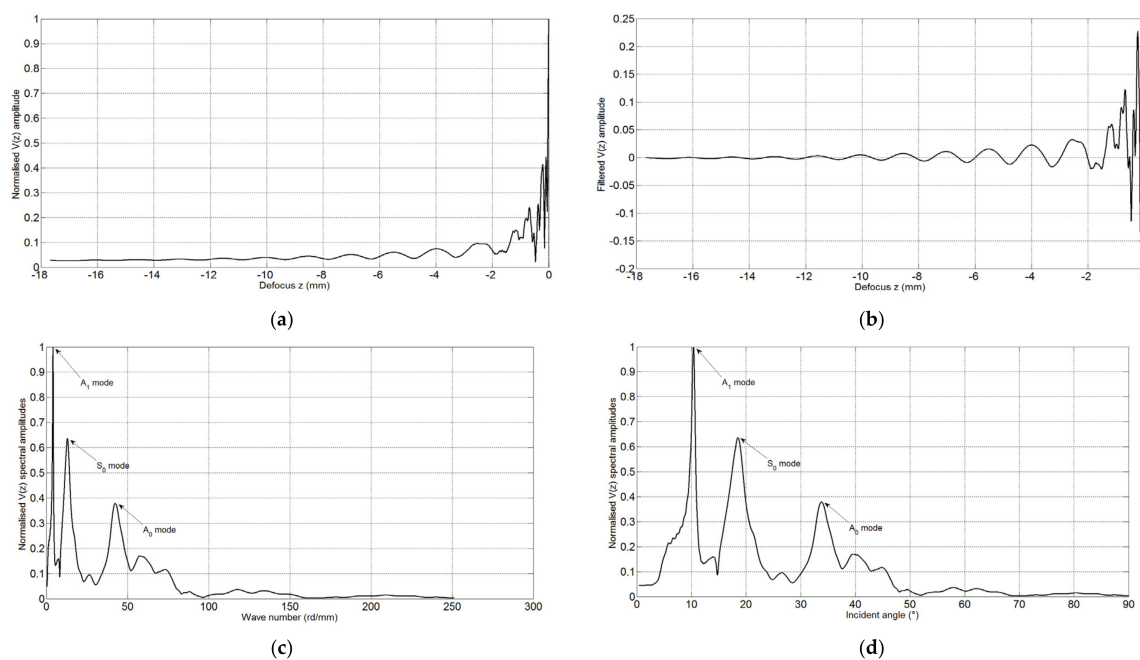where f is the working frequency of the piezoelectric element(s).

Figure 2. (**a**) Example of $V(z)$ curve of an aluminum plate; (**b**) corresponding filtered $V(z)$ curve; (**c**) spectral representation in the wave number space; (**d**) corresponding spectral representation in the incident angle space.

A high pass filtering technique is first used to eliminate the slowly decaying background, as illustrated in Figure 2b. Then, the periodicity Δz of oscillations is determined on the Fourier transform of the filtered $V(z)$ curve, which is then in the spatial domain of wave numbers k_s. Such a spectrum is represented in Figure 2c. Thus, each wave number value ξ_p associated with a peak in the spectrum corresponds to a leaky guided mode, and is linked to the periodicity Δz by:

$$\xi_p = \frac{2\pi}{\Delta z}.$$ (9)

The comparison between the modulus of the reflection coefficient and guided mode phase velocities is more convenient if a general abscissa ξ of the spectral component is defined, instead of the abscissa of the peaks ξ_p in Equation (9). Hence, the choice was made to adopt another representation of the $V(z)$ spectrum. Thus, replacing ξ_p by ξ from

Equation (9) into Equation (8), and the result into Equation (7), allows the spectrum of the $V(z)$ curves to be expressed as a function of an equivalent angle of incidence θ_0:

$$\theta_0 = \arcsin\left(\sqrt{1 - \left(1 - \frac{\xi}{4\pi f}V_0\right)^2}\right). \tag{10}$$

This angular spectral representation, as shown in Figure 2d, will be used from now on. It can be noticed that modes A_1, S_0, and A_0 are identified through the dispersion curves of the aluminum plate that will be studied hereafter in Section 3.2. It can also be noted that in regard to Equation (10) and Figure 2c,d, low wave numbers ξ correspond to low equivalent incident angles θ_0, and conversely.

As in Section 3.2 it will be required to identify the nature of Lamb modes polarization in an aluminum plate, we specify that their symmetric or antisymmetric nature, and their associated numbering (corresponding to the number of displacement nods inside the plate at the cut-off frequency of the modes), are obtained through their cut-off frequency value by the following principle:

For symmetric modes, the cut-off frequency values f_c are given by:

$$f_c.d = n.V_T \text{ , with } n \in \mathbb{N}^* \text{ for even symmetric modes } S_{2n}. \tag{11a}$$

$$f_c.d = \left(\frac{2n+1}{2}\right).V_L \text{ , with } n \in \mathbb{N} \text{ for odd symmetric modes } S_{2n+1} \tag{11b}$$

where d is the thickness of the plate, V_T and V_L are the shear and longitudinal wave velocities, respectively.

For antisymmetric modes, the cut-off frequency values f_c are given by:

$$f_c.d = n.V_L \text{ , with } n \in \mathbb{N}^* \text{ for even antisymmetric modes } A_{2n}. \tag{12a}$$

$$f_c.d = \left(\frac{2n+1}{2}\right).V_T \text{ , with } n \in \mathbb{N} \text{ for odd antisymmetric modes } A_{2n+1}. \tag{12b}$$

3. Results and Comparison

In this section, the guided wave velocities in a three-layer structure obtained with a classical $V(z)$ transducer and our new transducer design, are compared both in terms of reflection coefficients and corresponding dispersion curves. As mentioned in Section 2.3, this comparison will be facilitated by using Equations (7) and (10) in order to transform into the incident angle space, the dispersion curves, and guided wave velocity values, respectively.

3.1. Transducer and Material Properties

The piezoelectric element of the classical $V(z)$ transducer shown in Figure 1a is defined with a radius of curvature R_c of 25 mm and a half angular aperture θ_{ap} of 45°. Figure 1b shows the corresponding segmented $V(z)$ transducer with the same overall geometrical dimensions but where the piezoelectric element is segmented, each element being a strip with an angular aperture of 0.4°. Note that some companies propose, on demand, the design of such focused transducer whose dimensions are far away from those of state-of-the-art curved arrays. In Figure 1b, the segmented piezoelectric elements are sketched with a certain distance between them for clarity of illustration, but this distance is assumed to be negligible compared to the width of each segment. Thus, by activating several adjacent elements, a global and larger angular aperture up to several degrees can be defined. The resulting angular aperture is referred to as the "Rayleigh angular aperture" in the following sections. Indeed, since historically the $V(z)$ method was first used to generate Rayleigh waves in substrates, we used this denomination and extended it to the case of leaky Lamb waves. The frequency band of both transducers is assumed to be between 20 and 40 MHz.

Discussions will also be led at the end of this section for a transducer working in this frequency range, but with a smaller radius of curvature R_c.

We study the possibility to detect the guided waves in a three-layer structure, consisting of a top aluminum layer (70 μm thick), an epoxy layer (20 μm thick), and a steel layer (100 μm). For a given sample, the $V(z)$ signature depends, in particular, on its reflection coefficient R, that depends itself on the elastic parameters of the constitutive layers. Hence, the elastic constants and attenuations of these three layers, and those of the coupling fluid (water), are listed in Table 1, where the attenuation in epoxy is supposed to be constant while that in aluminum, steel, and water are assumed to be negligible in the considered frequency range. The attenuation in the epoxy layer is considered by taking into account an imaginary part in the longitudinal and shear wave vectors, respectively, k_L and k_T that appear in the reflection coefficient determination [35]. The elastic properties of aluminum and steel were measured by the authors, while those of epoxy were taken from [36].

Table 1. Material properties of aluminum, epoxy, steel, and water (coupling fluid).

Material	Mass Density (kg/m³)	Longitudinal Wave Velocity (m/s)	Transversal Wave Velocity (m/s)	Longitudinal Attenuation (Np/m)	Transverse Attenuation (Np/m)
Aluminum	2740	6190	3128	-	-
Epoxy	1548	2380	1400	20	53
Steel	7850	5940	3240	-	-
Water	1000	1500	-	-	-

3.2. Detection and Measurement of Guided Waves on the Three-Layer Structure

Figure 3a shows the modulus of the reflection coefficient of the three-layer structure between 0 and 50 MHz, and for incident angles that range from 0 to 50°, while Figure 3b shows the corresponding dispersion curves. The modulus of the reflection coefficient is not superimposed on the dispersion curves in order to allow the grey levels in the former to be observed. As a reminder, the details of the calculation of the reflection coefficient, as well as the one of the associated guided waves, can be found in [35].
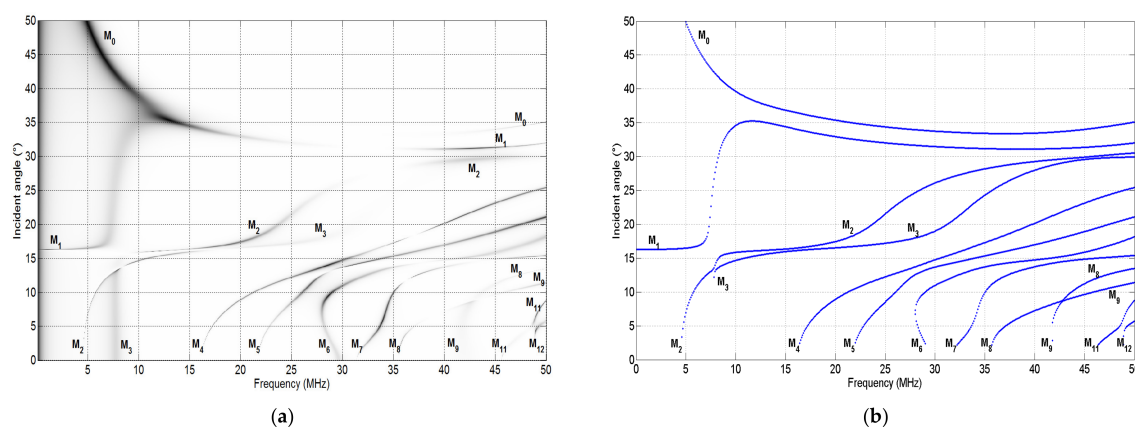

Figure 3. (**a**) Modulus of the reflection coefficient in the aluminum/epoxy/steel three-layer structure; (**b**) corresponding dispersion curves in the incident angle space.

The black color corresponds to the minima of the reflection coefficient (near zero) while the white color corresponds to the modulus of reflection coefficient equal to 1. The reflection coefficient is computed with its aluminum layer considered as the top surface that receives the incident plane wave from water. Indeed, due to attenuation in the epoxy layer, it should be noted that the reflection coefficient is not identical to the one obtained when reversing the order of layers according to the incident wave. Moreover, as the structure does not possess a symmetry plane, the guided waves are no longer symmetric or anti-symmetric. Thus, these modes cannot be named S or A as it is the case of a homogeneous plate, but

simply M, with an index (i) that is incremented according to the order of appearance of the mode when increasing the frequency, except for the M_0 and M_1 modes that do not possess a cut-off frequency. It should be noted that the angular axis is limited to 50° for clarity, but the M_1 mode tends toward 90° when frequency tends toward 0. In Figure 3a the label of certain modes was repeated near the final frequency values, when the corresponding resonant modes of the reflection coefficient seem to partially disappear, such as M_0, or seem to intersect, such as M_2 and M_3, which is not the case when looking at Figure 3b. It was also verified that M_8 and M_9 modes do not intersect near 42.8 MHz. The minima of the reflection coefficient modulus are found to be in excellent agreement with the positions of the free guided modes.

In order to further study the enhancement of detection and measurement of specific guided modes that correspond to propagation in specific layers of the three-layer structure, the guided modes of the whole structure and those (Lamb modes) of the constitutive layers taken separately are now studied. For this purpose, Figure 4 shows the superimposition of the dispersion curves in the three-layer structure with the Lamb wave curves in the aluminum layer (in green color) and steel layer (in red color), taken separately, which will be useful for further discussions. Each mode is here identified according to its nature, "S" for symmetric and "A" for anti-symmetric, with the superscript 'al' for aluminum and "st" for steel. Then, when defining a criterion corresponding to a maximum angular distance between modes, one can note that, for certain frequency ranges, some guided modes of the three-layer structure mostly correspond to Lamb modes that propagate in the aluminum layer, or in the steel one, taken separately. For example, when choosing a criterion of maximum angular distance between modes that is equal to 0.55°, the M_3 mode approximately corresponds to the S_0 mode of the aluminum layer, in the frequency range around 18 to 31 MHz. In the same manner, the M_1 mode approximately corresponds to the A_0 mode of the steel layer, in the frequency range around 20 to 40 MHz. Modes of the three-layer structure that do not match one of those of a single layer correspond to "coupling modes" that propagate inside the whole of the structure. It was verified that no guided modes correspond to Lamb modes of the epoxy layer in the frequency range from 0 to 50 MHz.
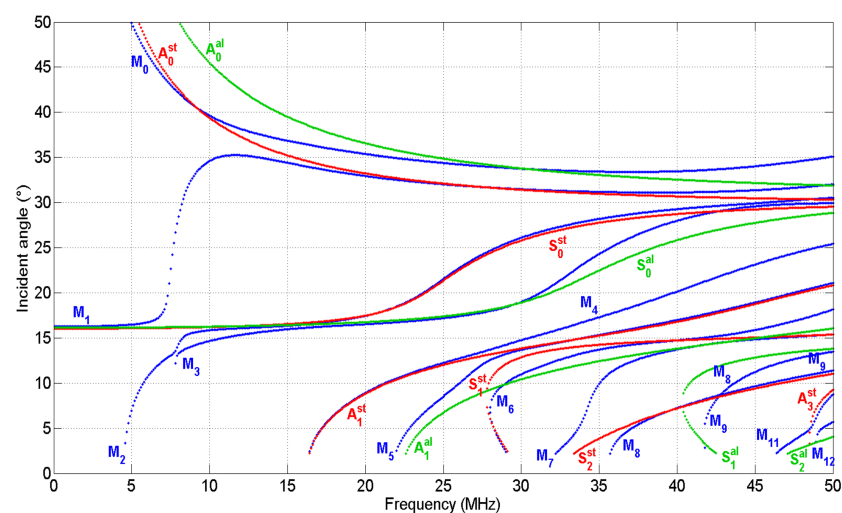

Figure 4. Superimposition of the dispersion curves of the three-layer structure (blue color) with the Lamb wave curves of the aluminum layer (green color) and steel layer (red color), considered separately.

Figure 5a,b represent the superimposition of the guided modes phase velocities that are detected with the classical $V(z)$ transducer in the frequency range 20–40 MHz, with the modulus of the reflection coefficient and with the dispersion curves, respectively. As in the case of our previous study of a single plate, we consider as detectable in the $V(z)$ spectra the guided modes that possess a peak with an amplitude at least twice the average amplitude

of the numerical noise in the spectrum. First, it can be observed that modes M_0, M_3, M_4, M_5, M_6, and M_7 are fairly well detected and determined, since their measured values are well superimposed on the corresponding guided modes of the dispersion curves. Figure 5a,b show that, except for M_7 mode, all the modes appearing for incident angles lower than about 7°, which correspond to phase velocities higher than approximately 12,308 m/s, cannot be detected. This is due to the fact that their low frequency spectral components are superimposed or "drowned" in the low frequency spectral components of the $V(z)$ curves. This is not the case for M_7 mode, which is detectable from about 4°, since it possesses a corresponding deep peak in the modulus of the reflection coefficient, as it can be observed when looking at its black trace in Figure 5a.
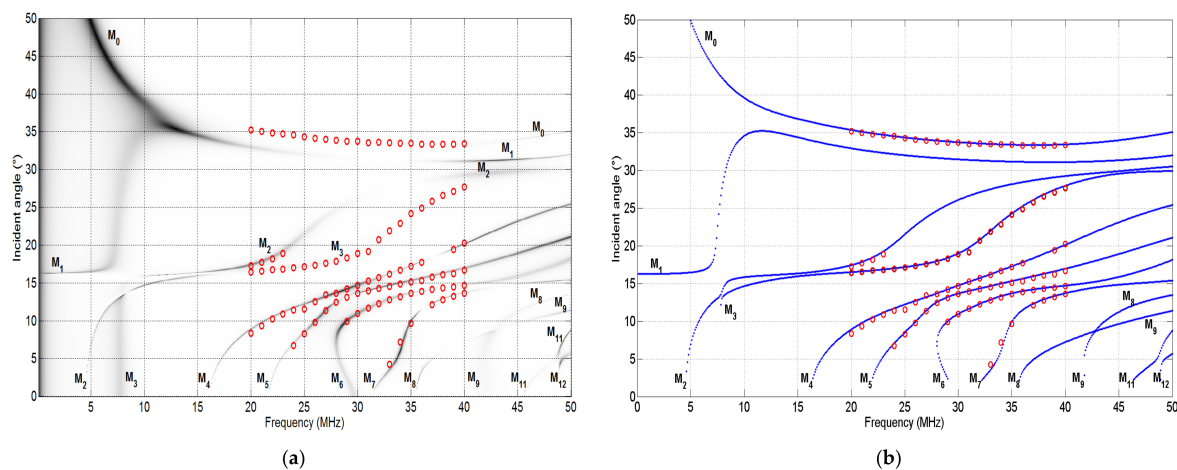

(a)   (b)

Figure 5. (**a**) Superimposition of the detected mode velocities (red circles), obtained with the classical $V(z)$ transducer, with the modulus of the reflection coefficient; (**b**) corresponding superimposition with the dispersion curves.

It can be noticed that the M_0 mode is almost unobservable in the minima of the modulus of reflection coefficient in Figure 5a, whereas its velocity values are well detected and determined with the classical $V(z)$ transducer over all the frequency range 20–40 MHz, as indicated in Figure 5b. An explanation for this is that, although its corresponding minimum in the reflection coefficient modulus is very small, and can even disappear, as illustrated at 25 MHz in Figure 6a, conversely, the last one continues to exhibit a large associated phase shift, as it can be seen in Figure 6b. This can be generalized to the entire frequency range from 20 to 40 MHz, as can be seen on the 3D views of the reflection coefficient's modulus and phase in Figure 6c,d, respectively. In these figures, for clarity, only the modes that we discuss are named. The theoretical positions of the M_0 mode peak are marked with white dots on the modulus of the reflection coefficient in Figure 6c to better compare them with the associated large phase shifts seen in Figure 6d. Concerning the M_1 mode, Figure 5a,b show that it is completely undetectable with the classical $V(z)$ transducer. This is due to a combination of two effects. Firstly, the neighboring M_0 mode is excited with more energy (due to its corresponding large phase shift in the reflection coefficient), and since it is very close to the M_1 mode, its spectral components in the $V(z)$ signal processing predominate and "drown" those of the M_1 mode. Secondly, the M_1 mode tends by itself to be less and less detectable with frequency, since its corresponding peak and phase shift in the reflection coefficient tend to decrease and become very small, as can be observed at 25 MHz in Figure 6a,b, respectively. Globally, the 3D view of Figure 6c shows that the peaks of the refection coefficient corresponding to the M_1 mode still exist between approximate frequency ranges 0–25 MHz and 35–40 MHz, but the associated phase shifts almost totally disappear in the frequency range 10–40 MHz, as illustrated in Figure 6d with white dots.
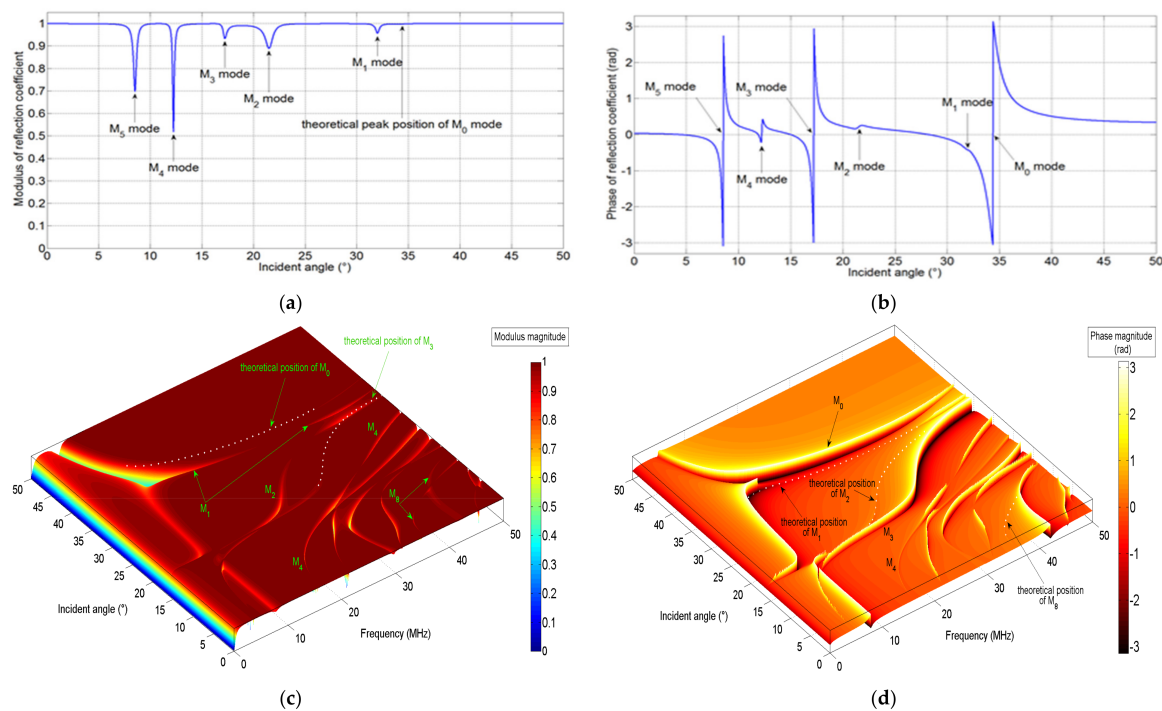
Figure 6. (**a**) Modulus of the reflection coefficient on the three-layer structure at 25 MHz; (**b**) corresponding phase of the reflection coefficient; (**c**,**d**) corresponding 3D global views of the modulus and phase of the reflection coefficient, respectively.

The M_2 mode is detectable for the first four frequency values (20 to 23 MHz), by tracking its corresponding spectral peak that starts around 17.3° at 20 MHz. However, its spectral peak rapidly decreases with frequency and becomes undetectable for frequencies higher than about 23 MHz, due to its corresponding peak and phase shift in the reflection coefficient that rapidly decrease and even disappear with frequency, as seen in Figure 6c,d, respectively. For M_3 mode, its corresponding peak in the modulus of reflection coefficient tends to disappear roughly between 30 MHz and 50 MHz, as illustrated in Figure 6c where the corresponding white dots show its theoretical position. However, its velocity values are well detected and determined with the classical $V(z)$ transducer over all the frequency range 20–40 MHz, as shown in Figure 5b. As for M_0 mode, this is due to its corresponding phase shift that is very large over all this frequency range, as illustrated in Figure 6d. It was verified that these results can be generalized: for a given mode, its corresponding phase shift has a predominant effect on its detection, compared to the associated peak of the modulus of the reflection coefficient. Thus, this conclusion can be applied to M_4 mode between roughly 37 and 38 MHz, and the totality of M_8 mode in the considered frequency range, which are not detected in these frequency ranges, as shown in Figure 5b. Indeed, Figure 6d shows that they possess a phase shift that vanishes in the aforementioned frequency ranges. White dots corresponding to M_8 mode curve are added in the frequency range 36–43 MHz, to better locate its theoretical position.

As explained above, M_2 mode is detectable only for the first four frequency values, while M_1 mode is completely undetectable. However, detection of M_1 mode, and a better detection of M_2 mode in the frequency range from 20 to 40 MHz would be of particular interest since they approximately correspond to modes in the steel layer, as represented in Figure 4. Indeed, assuming that this three-layer structure is mounted or clamped into a casing, $V(z)$ measurements will only be possible with the aluminum layer at the top surface. Thus, it would be interesting to detect these modes in order to characterize the elastic properties of the steel layer, which would correspond to a "buried" layer in such a configuration.

When trying to detect the M_1 mode with a segmented $V(z)$ transducer, one can note that for the considered frequency range, it possesses an angular variation lower than about $2°$, around an average value of $32°$. Thus, it is possible to choose a particular central angular aperture and most importantly a Rayleigh angular aperture that will be constant, since diffraction effects will allow to generate, and thus detect, this mode over its angular variation range. Trials have shown that a very good detection of its spectral peak is obtained for a central angular aperture of $2°$, and a Rayleigh angular aperture of $3°$, ranging between approximately $30°$ and $33°$. Figure 7a,b show the angular spectra of modes detected at 20 MHz, for the classical $V(z)$ transducer and segmented one, respectively. Attention must be paid to the fact that results for a classical $V(z)$ transducer are here given first, to facilitate further explanations. Indeed, knowing in advance the theoretical position of the M_1 mode with the help of the dispersion curves of Figure 5b, it is possible to indicate its position on the spectrum. Hence, one can observe in Figure 7a that it corresponds to a very low peak amplitude value, for example lower than the peaks of numerical artefacts appearing between 20 and 30 MHz.
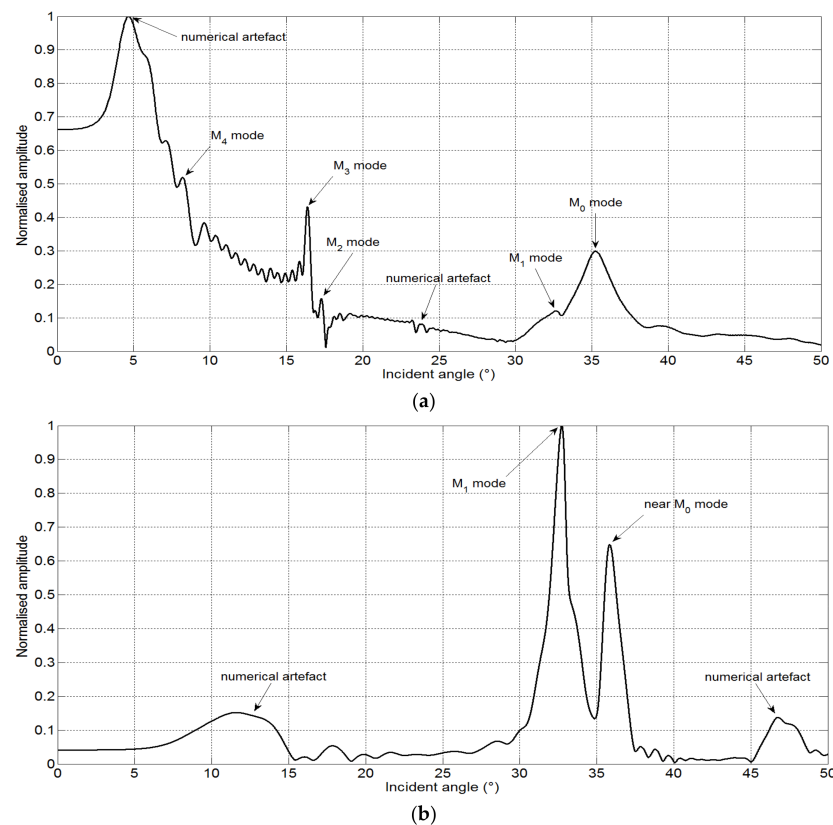

(a)

(b)

Figure 7. (**a**) Spectral representation of the modes detected at 20 MHz with the classical $V(z)$ transducer; (**b**) corresponding spectra obtained with the segmented $V(z)$ transducer.

Conversely, Figure 7b shows that this mode is very well detected with the segmented transducer with a corresponding peak that predominates. Figure 7b also shows that diffraction effects allow the M_0 mode to be detected, but with a lower precision than for the case of the classical $V(z)$ transducer. This is due to the angular proximity of M_0 and M_1 modes, and the relatively large peak of mode M_1 whose spectral components disturbs the repartition of the M_0 spectral ones. It is then possible to follow the peak of the M_1 mode over the frequency range from 20 up to 30 MHz with a step of 1 MHz, using the segmented $V(z)$ transducer. Its spectral peak becomes undetectable in the frequency range from about 30 to 33 MHz, due to its too small corresponding peak and phase shift in the reflection coefficient, and then becomes again detectable from 34 MHz upwards, since its corresponding phase shift reappears, as observed in Figure 6d.

One can also notice the presence of numerical artefacts on these spectra. As far as the classical $V(z)$ transducer is concerned (Figure 7a), it was verified that the numerical artefact located near the low incident angle values approximately centered around 5 degrees, corresponds to a part of spectral components ζ that are just after the continuous one. As a reminder, as illustrated in Figure 2b,c, low incident angles $\theta_0°$ also correspond to low wave numbers ζ. Thus, these components remain present after applying a high pass filter, but, if desired, can be eliminated by increasing the cut-off frequency. Concerning the numerical artefacts of Figure 7b for the segmented $V(z)$ transducer, they appear approximately around 12 degrees and 43 degrees, respectively. It was verified that they never appear at such levels of amplitude when using a classical $V(z)$ transducer. These artefacts can be attributed to the diffraction effects of the piezoelectric segments that are activated, which generate multiple echoes inside the three-layer structure and, in steady state, radiate their energy around specific wave numbers, or equivalently, specific incident angles. Due to the design of the segmented $V(z)$ transducer that allows one to select the modes that one wishes to detect, and thus to isolate the position of their peaks; these numerical artefacts are always outside the region of interest. Hence, they do not impact the determination of the spectral peaks position. Moreover, they could even be removed by applying a second filter of band-pass type, centered around the peak positions of the selected modes.

This method allows for the angular position of M_0 mode, and more importantly of M_1 mode, to be detected, as represented in Figure 8a,b with orange crosses for M_0 and M_1. These figures represent the superimposition of this detected mode with the modulus of the reflection coefficient and dispersion curves, respectively. It thus can be observed in Figure 8b that M_1 mode is clearly detected and superimposes well on the corresponding dispersion curve. Results concerning the generation and detection of the M_2 mode with a segmented transducer are also added on Figure 8a,b, and will be discussed below.
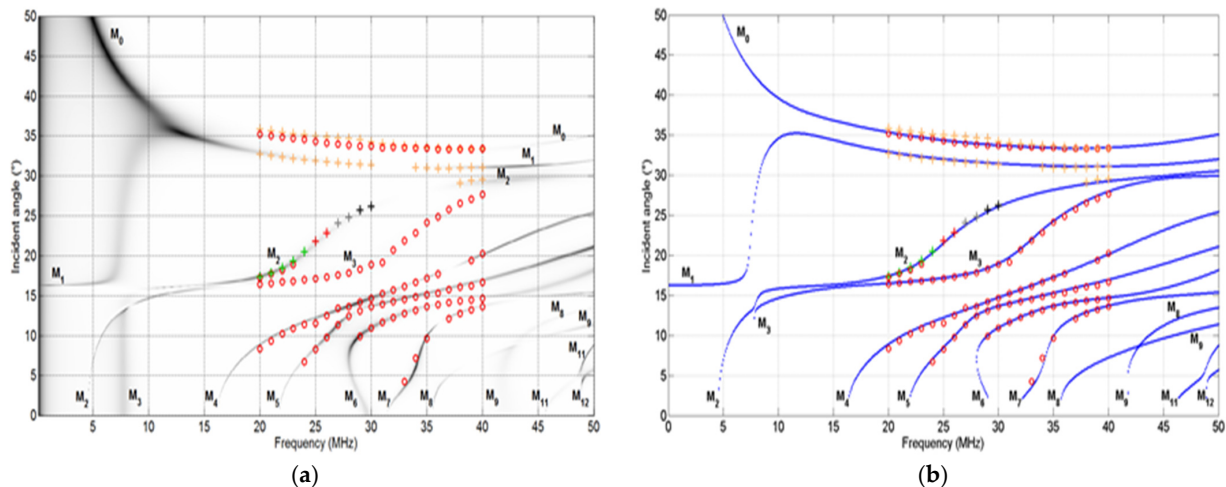

Figure 8. (**a**) Superimposition of all the mode velocities, generated and detected with the classical *V(z)* transducer (circles) and the segmented one (crosses), with the modulus of the reflection coefficient; (**b**) corresponding superimposition with the dispersion curves.

Unlike the M_1 mode, the M_2 mode varies with a relatively large angular range of about $12°$. Thus, even when taking into account diffraction effects, it is impossible to detect and track it with a fixed Rayleigh aperture angle all along the frequency range from 20 to 40 MHz. The method we have developed here consists of searching at start the best Rayleigh aperture values at the first frequency value of 20 MHz, corresponding to a peak of the M_2 mode that predominates in the angular spectrum. It was found that a central aperture angle of $2°$ and a Rayleigh aperture comprised between $18°$ and $20°$ allow a predominant peak of the M_2 mode at 20 MHz to be obtained. This leads to the spectrum represented in Figure 9a, while Figure 7a is repeated as Figure 9b for comparison with the spectrum obtained with the classical $V(z)$ transducer. Then, the idea consists of

gradually increasing the frequency, in small steps, and, when necessary, increasing the angular aperture position (while keeping a 2° aperture value) in order to continuously track the position of M_2 peak.
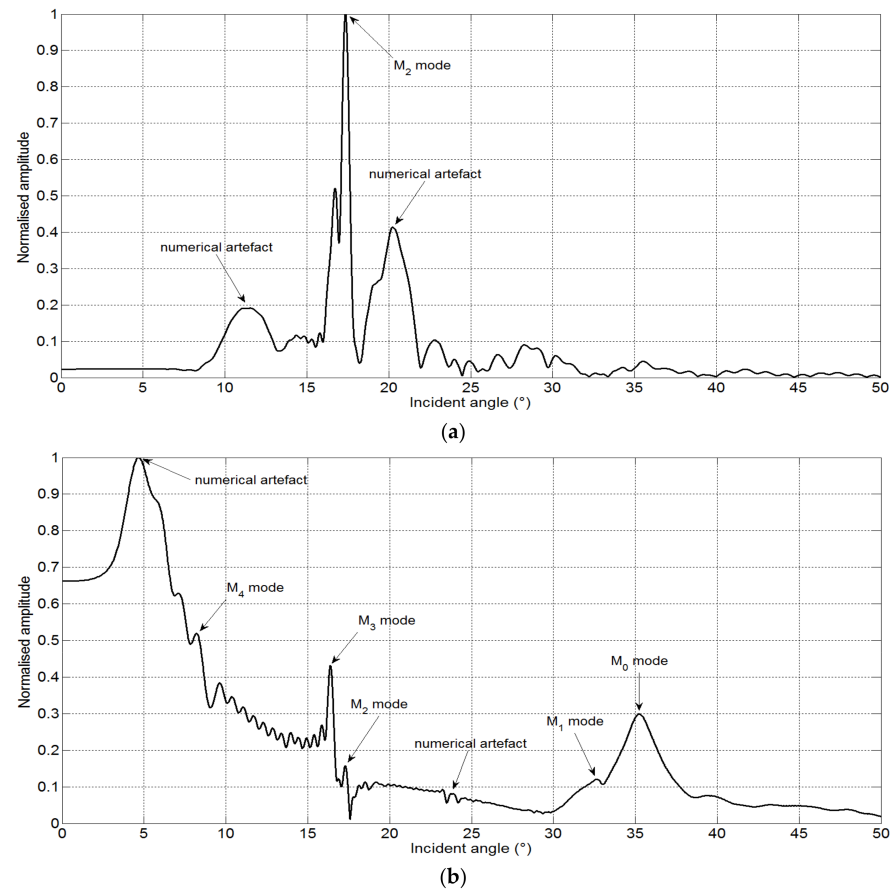

(**a**)

(**b**)

Figure 9. (**a**) Spectral representation of modes detected at 20 MHz with the segmented $V(z)$ transducer; (**b**) corresponding spectra obtained with the classical $V(z)$ transducer.

In practice, as the curve of the M_2 mode starts at 20 MHz with a small slope, the initial segmented transducer configuration allows to detect it from 20 up to 24 MHz, as represented by the five green crosses in Figure 8a,b. It can be noted that the first four values are measured with a better accuracy than the ones measured with a classical $V(z)$ transducer. Then, it was found that an angular aperture position shifted by 2 degrees every 2 MHz was a good criterion to track the position of the M_2 peak. For instance, in the frequency range from 25 to 26 MHz, the angular aperture position is shifted between 20° and 22°, corresponding to the two red crosses in Figure 8a,b. In the frequency range from 27 to 28 MHz, it corresponds to an angular aperture position shifted between 22° and 24°, corresponding to the two grey crosses, and so on. This method allows the M_2 mode to be detected up to 30 MHz, while only up to 24 MHz with the classical $V(z)$ transducer. Between roughly 31 and 37 MHz, M_2 mode becomes undetectable even with the segmented $V(z)$ transducer, since it corresponds to peaks (lack of black trace) in the modulus of the reflection coefficient and phase shifts that completely vanish, as observed in Figure 6c,d, respectively. Although this mode theoretically exists in the dispersion curves and for this frequency range, it corresponds in practice to a mode that requires a lot of energy to be generated, and/or that leaks too little energy in water to be detected. As represented in Figure 8a,b by the last three brown crosses, M_2 mode becomes detectable again for frequencies from about 38 to 40 MHz (three orange crosses), but measured with low precision due to the presence of the neighboring M_1 mode that disturbs the spectral components of its peak.

Other simulations were performed with a segmented $V(z)$ transducer having a radius of curvature R_c of 15 mm, and then 10 mm. Even with these values, it was verified that the previous results globally still hold. Indeed, the detected M_1 and M_2 modes correspond to relatively high incident angles, i.e., to low phase velocities (see Equation (7)), which corresponds to small periods of oscillations Δz (see Equation (8)) in the $V(z)$ curves. Thus, even if the radius of curvature is decreased, leading to a lower extent of defocus values in the $V(z)$ curves, the number of periods is still high enough to be correctly estimated in the corresponding spectra. The main difference that was observed, compared to the results with the initial radius of curvature of 25 mm, is the fact that some modes are detected in a slightly smaller frequency range. For instance, it was verified that the M_1 mode remains undetectable in a frequency range from about 28 up to 35 MHz for a radius of curvature R_c of 15 mm, and from about 26 up to 36 MHz for a radius of curvature of 10 mm.

A last remark must be made concerning the thicknesses of the structure studied here and the frequency range. As it is well known, the reflection coefficient and the dispersion curves only depend on the frequency-thickness product. So, in principle, all the results would have been the same by multiplying all the thicknesses by 10 and dividing the frequency values by 10, leading to a frequency range of 0 to 5 MHz. However, we found that this leads to inaccurate results in terms of detection and measurements of M_1 and M_2 modes with the same geometry of segmented $V(z)$ transducer, due to the increase in diffraction effects at low frequencies. For these modes, the acoustical energy that is emitted by the segmented $V(z)$ transducer in the direction of the incident angles of the M_1 and M_2 modes is lower than previously (for the frequency range from 20 to 40 MHz) since a part of it is spread in other directions. Since these modes are excited with less energy, their peaks do not sufficiently stand out in the spectrum to be accurately measured or even detected. Concerning more specifically M_1 mode in the frequency range 0–5 MHz, diffraction effects also imply that more energy is leaked and absorbed by its neighboring M_0 mode, whose spectral peak components predominate again and tend to "drown" those of M_1.

4. Conclusions

Using a new concept of segmented—or multi-element—$V(z)$ transducer, this work illustrates the possibility of detection and measurement of leaky guided modes in multilayered structures, that are difficult-or impossible-to generate with a classical $V(z)$ transducer, and/or that reradiate only little energy in the coupling fluid. The modeling of the generalized $V(z)$ signature for a segmented $V(z)$ transducer was first performed, then a three-layer structure was considered. This structure, composed of aluminum (0.07 mm), epoxy (0.02 mm) and steel (0.1 mm), was studied in the frequency range from 20 to 40 MHz. It was shown that with a classical $V(z)$ transducer, the two modes M_1 and M_2—corresponding to modes in the "buried" steel layer in the frequency range between 20 and 40 MHz—are not (or poorly) detected in the $V(z)$ spectra, due to too small corresponding minimum and/or phase shift in the associated reflection coefficient. Contrary to this situation, the segmented $V(z)$ transducer allows these guided modes to be detected and correctly measured in this frequency range. As M_1 mode possesses a small angular variation for frequencies up to 20 MHz, it is possible to set the range of Rayleigh angles once and for all for the entire frequency range, since diffraction effects allow to spread acoustical energy in an incident angle range large enough to cover all the corresponding incident angle values. Unlike M_1 mode, M_2 mode possesses a large angular variation in the frequency range from 20 to 40 MHz. Thus, when searching to complete its detection with the segmented $V(z)$ transducer, it is impossible to maintain a constant range of Rayleigh angles over this frequency domain. In this case, an original technique was developed. It consists of searching the best initial configuration of the segmented transducer for the first frequency value, in order to obtain the largest corresponding peak in the spectrum of $V(z)$ curve. Then, the Rayleigh angles range is kept constant as long as the corresponding peak of M_2 mode is predominant in the spectrum. When it becomes lower than another spectral peak, the Rayleigh angles range is progressively increased until the peak of M_2 becomes again the predominant one. This

method allows the M_2 mode to be detected and tracked up to 30 MHz, while only 24 MHz can be reached with the classical $V(z)$ transducer.

It is shown that diffraction effects, that appear when using segmented $V(z)$ transducers, possess advantages and disadvantages. Indeed, for modes such as M_1 of the three-layer structure studied here and possessing a small angular variation for a given high enough frequency range, they allow to maintain the Rayleigh angles range constant over this frequency range for modes detection. However, when working at much lower frequencies (roughly ten times lower), the diffraction effects increase and become an inconvenient. Indeed, they spread the radiated energy, and thus decrease the energy absorbed by the mode that is desired to be generated and detected. This leads to inaccurate results in terms of detection and measurements of modes that are excited with too little energy, as it was verified to be the case for the M_1 and M_2 modes when using a frequency range from 0 to 5 MHz.

When the previous conditions are fulfilled, it was shown that there is no need for a precise knowledge of the angular position of a mode in order to detect it. Indeed, thanks to diffraction effects, only an initial guess of the angular position is required to choose the range of angular apertures of piezoelectric elements that can excite the mode. This can be of great practical interest for precise elastic constant characterization, since only a rough estimation of these constants is often known in advance, implying an unknown precise position of corresponding guided modes generation angle.

Finally, the technologies required to fabricate our segmented $V(z)$ transducer are quite similar to those used for a standard curved array and are already available. Thus, our approach is of particular interest in practice, especially when such guided modes (modes M_1 and M_2 in our example) correspond to a specific layer that needs to be characterized, but not directly accessible, such as a "buried" layer, or a bottom layer in a structure that cannot be reversed for practical reasons.

Author Contributions: Conceptualization, M.L. (Michaël Lematre) and M.L. (Marc Lethiecq); methodology, M.L. (Michaël Lematre) and M.L. (Marc Lethiecq); software, M.L. (Michaël Lematre); validation, M.L. (Michaël Lematre) and M.L. (Marc Lethiecq); formal analysis, M.L. (Michaël Lematre); investigation, M.L. (Michaël Lematre); resources, M.L. (Michaël Lematre); writing—original draft preparation, M.L. (Michaël Lematre); writing—review and editing, M.L. (Michaël Lematre) and M.L. (Marc Lethiecq); visualization, M.L. (Michaël Lematre); supervision, M.L. (Michaël Lematre) and M.L. (Marc Lethiecq); project administration, M.L. (Marc Lethiecq) All authors have read and agreed to the published version of the manuscript.

Data Availability Statement: Data available on request from the authors.

Conflicts of Interest: The authors declare no conflict of interest.

References

1. Rokhlin, S.I.; Huang, W. Ultrasonic wave interaction with a thin anisotropic layer between two anisotropic solids: Exact and asymptotic-boundary-condition methods. *J. Acoust. Soc. Am.* **1992**, *92*, 1729–1742. [CrossRef]
2. Ismaili, N.A.; Chenouni, D.; Lakhliai, Z.; El-Kettani, M.E.C.; Morvan, B.; Izbicki, J.L. Determination of epoxy film parameters in a three-layer metal/adhesive/metal structure. *IEEE Trans. Ultrason. Ferroelectr. Freq. Control* **2009**, *56*, 1955–1959. [CrossRef] [PubMed]
3. Mustapha, S.; Ye, L. Propagation behaviour of guided waves in tapered sandwich structures and debonding identification using time reversal. *Wave Motion* **2015**, *57*, 154–170. [CrossRef]
4. Balvantín, A.J.; Diosdado-De-la-Peña, J.A.; Limon-Leyva, P.A.; Hernández-Rodríguez, E. Study of guided wave propagation on a plate between two solid bodies with imperfect contact conditions. *Ultrasonics* **2018**, *83*, 137–145. [CrossRef] [PubMed]
5. Guo, Z.; Achenbach, J.D.; Madan, A.; Martin, K.; Graham, M.E. Modeling and acoustic microscopy measurements for evaluation of the adhesion between a film and a substrate. *Thin Solid Films* **2001**, *394*, 188–200. [CrossRef]
6. Baltazar, A.; Wang, L.; Xie, B.; Rokhlin, S.I. Inverse ultrasonic determination of imperfect interfaces and bulk properties of a layer between two solids. *J. Acoust. Soc. Am.* **2003**, *114*, 1424–1434. [CrossRef]
7. Boström, A.; Golub, M. Elastic SH wave propagation in a layered anisotropic plate with interface damage modelled by spring boundary conditions. *Q. J. Mech. Appl. Math.* **2009**, *62*, 39–52. [CrossRef]

8. Golub, M. Propagation of elastic waves in layered composites with microdefect concentration zones and their simulation with spring boundary conditions. *Acoust. Phys.* **2010**, *56*, 848–855. [CrossRef]

9. Leiderman, R.; Figueroa, J.C.; Braga, A.M.B.; Rochinha, F.A. Scattering of ultrasonic guided waves by heterogeneous interfaces in elastic multi-layered structures. *Wave Motion* **2016**, *63*, 68–82. [CrossRef]

10. Leiderman, R.; Braga, A.M.B. Scattering of guided waves by defective adhesive bonds in multilayer anisotropic plates. *Wave Motion* **2017**, *74*, 93–104. [CrossRef]

11. Siryabe, E.; Rénier, M.; Meziane, A.; Galy, J.; Castaings, M. Apparent anisotropy of adhesive bonds with weak adhesion and non-destructive evaluation of interfacial properties. *Ultrasonics* **2017**, *79*, 34–51. [CrossRef] [PubMed]

12. Fraisse, P.; Schmit, F.; Zarembowitch, A. Ultrasonic inspection of very thin adhesive layers. *J. Appl. Phys.* **1992**, *72*, 3264–3271. [CrossRef]

13. Xu, P.C.; Lindenschmidt, K.E.; Meguid, S.A. A new high-frequency analysis of coatings using leaky lamb waves. *J. Acoust. Soc. Am.* **1993**, *94*, 2954–2962. [CrossRef]

14. Rogers, J.A.; Dhar, L.; Nelson, K.A. Noncontact determination of transverse isotropic elastic moduli in polyimide thin films using a laser based ultrasonic method. *Appl. Phys. Lett.* **1994**, *65*, 312–314. [CrossRef]

15. Rokhlin, S.I.; Ganor, M.; Degtyar, A.D. Ultrasonic characterization of plasma spray coating. In *Review of Progress in Quantitative Nondestructive Evaluation*; Springer: New York, NY, USA, 1997; pp. 1585–1591. [CrossRef]

16. Van de Rostyne, K.; Glorieux, C.; Gao, W.; Gusev, V.; Nesladek, M.; Lauriks, W.; Thoen, J. Investigation of elastic properties of CVD-diamond films using the lowest order flexural leaky lamb wave. *Phys. Stat. Sol. A* **1999**, *172*, 105–111. [CrossRef]

17. Alleyne, D.; Cawley, P. A 2-dimensional Fourier transform method for the measurement of propagating multimode signals. *J. Acoust. Soc. Am.* **1991**, *89*, 1159–1168. [CrossRef]

18. Abbate, A.; Koay, J.; Frankel, J.; Schroeder, S.C.; Das, P. Application of wavelet transform signal processor to ultrasound. *Proc. IEEE Ultrason. Symp.* **1994**, *2*, 1147–1152. [CrossRef]

19. Titov, S.A.; Maev, R.G.; Bogachenkov, A. Measurements of velocity and attenuation of leaky waves using an ultrasonic array. *Ultrasonics* **2006**, *44*, 182–187. [CrossRef]

20. Titov, S.A.; Maev, R.G.; Bogachenkov, A. Lens multielement acoustic microscope in the mode for measuring the parameters of layered objects. *Acoust. Phys.* **2017**, *63*, 583–589. [CrossRef]

21. Titov, S.A.; Maev, R.G. An Ultrasonic Array Technique for Material Characterization of Plate Samples. *IEEE Trans. Ultrason. Ferroelectr. Freq. Control* **2013**, *60*, 1435–1445. [CrossRef]

22. Lemons, R.A.; Quate, C.F. Acoustic microscope. *Phys. Acoust.* **1979**, *XIV*, 1. [CrossRef]

23. Kushibiki, J.I.; Chubachi, N. Material characterization by line-focus beam acoustic microscopy. *IEEE Trans. Son. Ultrason.* **1985**, *32*, 189–212. [CrossRef]

24. Nayfeh, H.; Chimenti, D.E. Propagation of guided waves in fluid-coupled plates of fiber-reinforced composite. *J. Acoust. Soc. Am.* **1988**, *83*, 1736–1743. [CrossRef]

25. Nagy, P.B.; Adler, L. Adhesive joint characterization by leaky guided interface waves. In *Review of Progress in Quantitative Nondestructive Evaluation*; Springer: New York, NY, USA, 1989; pp. 1417–1424. [CrossRef]

26. Philibert, M.; Yao; Gresil, M.; Soutis, C. Lamb waves-based technologies for structural health monitoring of composite structures for aircraft applications. *Eur. J. Mater.* **2022**, *2*, 436–474. [CrossRef]

27. Gorgin, R.; Luo, Y.; Wu, Z. Environmental and operational conditions effects on Lamb wave based structural health monitoring systems: A review. *Ultrasonics* **2020**, *105*, 106114. [CrossRef]

28. Liu, G.R.; Achenbach, J.D.; Kim, J.O.; Li, Z.I. A combined finite element method/boundary element method technique for V(z) curves of anisotropic-layer/substrate configurations. *J. Acoust. Soc. Am.* **1992**, *92*, 2734–2740. [CrossRef]

29. Lee, Y.C.; Kim, J.O.; Achenbach, J.D. V(z) curves of layered anisotropic materials for the line-focus acoustic microscope. *J. Acoust. Soc. Am.* **1993**, *94*, 923–930. [CrossRef]

30. Achenbach, J.D.; Kim, J.O.; Li, W. Measuring thin-film elastic constants by line-focus acoustic microscopy. *Adv. Acoust. Micros.* **1995**, *129*, 153–208. [CrossRef]

31. Guo, Z.; Achenbach, J.D.; Madan, A.; Martin, K.; Graham, M.E. Integration of modeling and acoustic microscopy measurements for thin films. *J. Acoust. Soc. Am.* **2000**, *107*, 2462–2471. [CrossRef]

32. Lee, Y.C.; Cheng, S.W. Measuring Lamb wave dispersion curves of a bi-layered plate and its application on material characterization of coating. *IEEE Trans. Ultrason. Ferroelectr. Freq. Control* **2001**, *48*, 830–837. [CrossRef]

33. Bourse, G.; Xu, W.J.; Mouftiez, A.; Vandevoorde, L.; Ourak, M. Interfacial adhesion characterization of plasma coatings by V(z) inversion technique and comparison to interfacial indentation. *NDT E Int.* **2012**, *45*, 22–31. [CrossRef]

34. Lematre, M.; Benmehrez, Y.; Bourse, G.; Xu, W.J.; Ourak, M. Acoustic microscopy measurement of elastic constants by using an optimization method on measured and calculated SAW velocities: Effect of initial C_{ij} values on the calculation convergence. *NDT E Int.* **2002**, *35*, 279–286. [CrossRef]

35. Loukkal, A.; Lematre, M.; Bavencoffe, M.; Lethiecq, M. Modeling and numerical study of the influence of imperfect interface properties on the reflectance function for isotropic multilayered structures. *Ultrasonics* **2020**, *103*, 106099. [CrossRef] [PubMed]

36. Vijaya Kumar, R.I.; Bhat, M.R.; Murthy, C.R.I. Some studies on evaluation of degradation in composite adhesive joints using ultrasonic techniques. *Ultrasonics* **2013**, *53*, 1150–1162. [CrossRef] [PubMed]